ACS OMEGA

Open Access

http://pubs.acs.org/journal/acsodf

Article

Probing Active Sites on Pristine and Defective $MnPX_3$ (X: S and Se) Monolayers for Electrocatalytic Water Splitting

Jiajun Dai,* Kangli Wang, Elena Voloshina,* Yuriy Dedkov,* and Beate Paulus

Cite This: *ACS Omega* 2023, 8, 33920−33927

Read Online

ACCESS | Metrics & More | Article Recommendations | Supporting Information

ABSTRACT: The state-of-the-art density functional theory approach was used to study the structural and electronic properties of pristine and defective $MnPX_3$ monolayers as well as their activity toward water and hydrogen evolution reaction (HER) catalytic performance. The adsorption behavior of H_2O on a pristine $MnPX_3$ structure is of physisorption nature, whereas the adsorption energy is significantly increased for the defective structures. At the same time, the water dissociation process is more energetically favorable, and the reactivity of $MnPX_3$ is determined by the vacancy configuration. Following Nørskov's approach, the HER catalytic performance is evaluated by calculating the hydrogen adsorption free energy on the respective $MnPX_3$ surface. Our calculation results demonstrate that defective 2D $MnPX_3$ with low coordinated P shows significantly higher HER performance compared to the pristine counterpart.

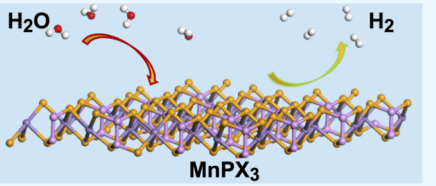

INTRODUCTION

Green and renewable energy, generated from natural resources, such as sunlight, wind, or water, has become a hot topic due to the extremely severe environmental pollution and energy dilemma.[1] In this regard, carbon-free hydrogen fuel,[2,3] which can be produced without any incidental contamination by electrochemical water splitting driven by clean electricity generated directly or indirectly from sustainable energy sources, has attracted wide attention around the world. The electrochemical water splitting reaction has two components—hydrogen evolution reaction (HER) and oxygen evolution reaction (OER). HER is the reaction where hydrogen, H_2, is generated *via* the reduction of the proton, H^+, at the cathode, and OER is the reaction where oxygen, O_2, is generated *via* the oxidation of the hydroxyl ion, OH^-, at the anode. At present, the most advanced catalysts are still mostly composed of very expensive noble metals or their oxides, such as Pt for HER and RuO_2 for OER. Therefore, it is necessary to develop new affordable alternative catalysts with comparative catalytic performance.[4] Thus, the current research in the field of electrocatalysis or photocatalysis is mainly focused on the study of new electrochemical catalysts to accelerate the kinetics and minimize the overpotential due to poor electrochemical performance.[5,6]

Since the unique transport properties of graphene were first reported in 2004,[7] 2D materials have emerged in various research fields,[8−13] including electrocatalysis.[14] This is not surprising since 2D nanomaterials have a more uniform open crystal lattice compared to other materials such as nanoporous materials or nanotubes and achieve a higher concentration of open electrocatalytic active sites.[15] An additional motivation to employ 2D materials in electrocatalytic applications is that they are typically inexpensive. Following many experimental and theoretical works on 2D materials and the respective interest to renewable energy sources, in the past decade, significant attention is given to van der Waals layered materials known as transition metal trichalcogenides (MPX_3 with M: transition metal and X: S or Se).[16−28] From the crystallographic point of view, these materials are similar to transition metal dichalcogenides, MX_2, where one-third of the metal cations with connected X-anions is substituted by an ethane-like $[P_2X_6]^{4-}$ unit (Figure 1a,b). The diversity in transition metals and two different chalcogens can lead to a wide variation in the electronic and magnetic properties of these materials,[29−31] which can be further tailored by applying stress,[32] an external voltage gate,[16,33] or by alloying.[34,35] Due to the layered structure of MPX_3, they can be easily prepared as two-dimensional nanostructures[36,37] with a large surface area and high number of active sites.[27,38−40] Consequently, the MPX_3 materials have been the subject of several application-related investigations,[22,38,39,41,42] and $FePSe_3$ and $MnPSe_3$ yielded the highest efficiency for HER and very good stability in a wide pH range. At that, the existing theoretical and experimental works, focused on the electrocatalytic properties of MPX_3, very rarely contain an insight in the electronic structure, which is crucial for understanding and controllable modification of the catalytic activity of these materials.

In this work, we investigate the structural, electronic, water adsorption, and HER properties of pristine and defective 2D $MnPX_3$ (X: S and Se). We first studied the electronic and

Received: June 30, 2023
Accepted: August 11, 2023
Published: September 5, 2023

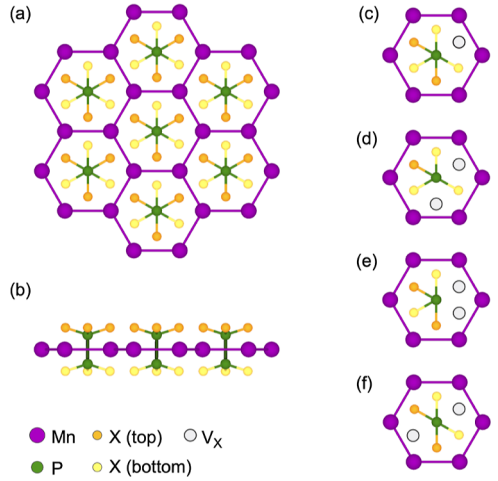

Figure 1. (a) Top and (b) side views of a single layer of MPX_3. (c–f) Structure of the considered chalcogen defects: (c) V_X@1L; (d) V_{X2}@1L; (e) V_{X2a}@2L; and (f) V_{X2b}@2L. Spheres of different sizes/colors represent ions of different types.

magnetic structure of the pristine and defective structures with different vacancy configurations. Then, their reactivity toward water was examined to probe the active centers and investigate the influence of defects. At the final step, the HER catalytic performance is predicted by calculating hydrogen adsorption free energy to understand the catalytic mechanism.

RESULTS AND DISCUSSION

When considering 2D $MnPX_3$ (X: S and Se) monolayers (Figure 1a,b), their energetically most favorable structures correspond to the Néel antiferromagnetic (nAFM) arrangement of magnetic moments. Both monolayers under study are direct band gap semiconductors: the valence band maximum and the conduction band minimum are located at the *K* point (see Figure S1 of the Supporting Information). The band gaps obtained in this work are E_g = 2.47 and 1.81 eV for $MnPS_3$ (Figure 2a) and $MnPSe_3$ (Figure 2b), respectively, and they are in agreement with previously published results.[33,43] At that, the top of the valence band is mainly formed by S/Se p-states with a significant contribution form the Mn d-states, whereas the bottom of the conduction band is contributed by Mn, P, and S/Se states (Figure 2a,b). Thus, both systems under study can be assigned to the class of Mott–Hubbard-type insulators, similarly to $FePX_3$.[28,30]

The mechanical exfoliation used for monolayer production can lead to the formation of chalcogen vacancies. Therefore, we consider four different kinds of defects: one vacancy at the X-site, named as V_X@1L (Figure 1c) with a defect concentration of about 2.5%, two vacancies at the neighboring X-sites of the same chalcogen sublayer named as V_{X2}@1L (Figure 1d) with a concentration of about 5%, and two vacancies at the X-sites of the different chalcogen sublayers named as V_{X2a}@2L (Figure 1e) and V_{X2b}@2L (Figure 1f) with a concentration of about 5%. The defect formation energies (ΔE_{def}) are listed in Table 1. Overall, ΔE_{def} are in the same range as those of other MPX_3.[28,36,37] For the same defect type,

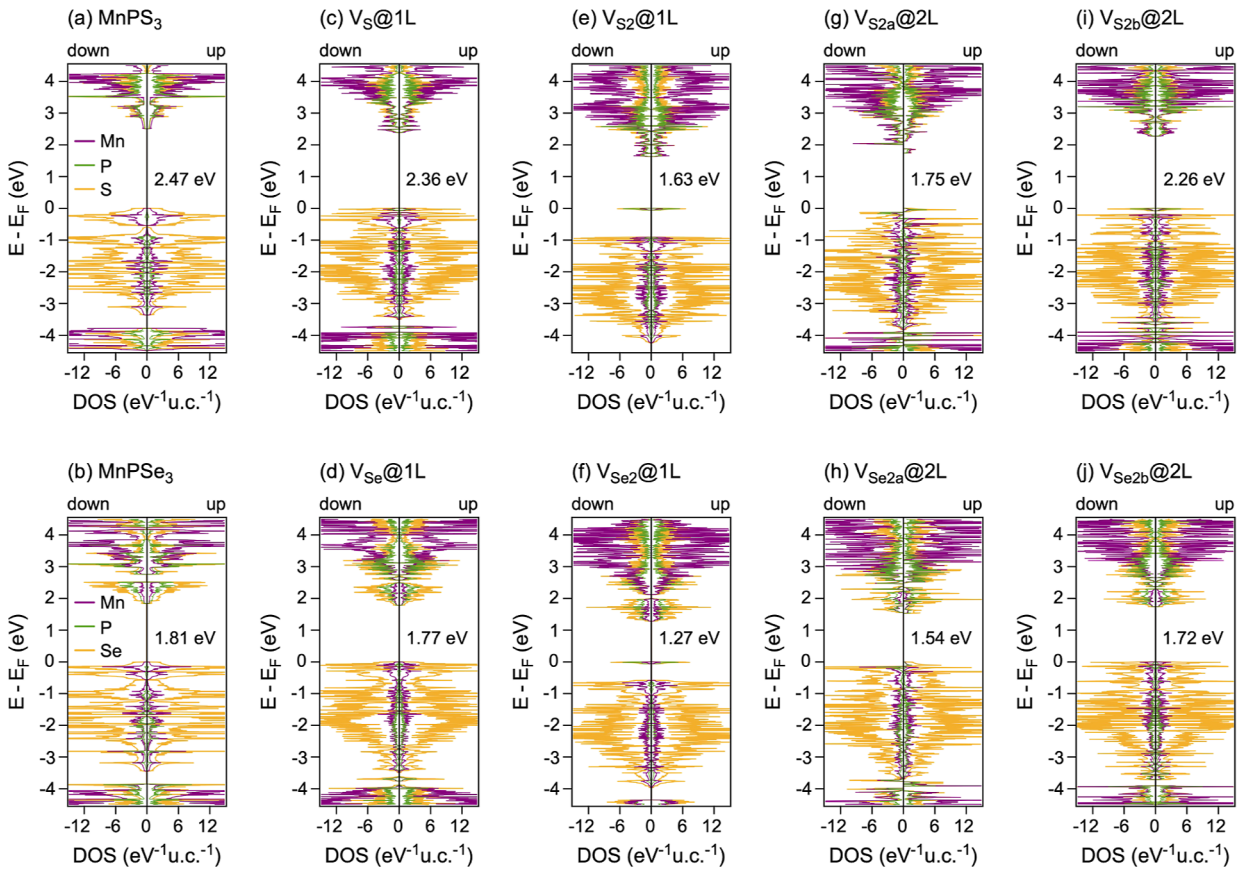

Figure 2. Atom-projected density of states calculated with PBE + *U* + D2 for (a,b) pristine $MnPX_3$ and (c–j) defective $MnPX_3$ (X: S and Se). The band gap width is indicated at each subplot.

https://doi.org/10.1021/acsomega.3c04677
ACS Omega 2023, 8, 33920–33927

Table 1. Defect Formation Energies (in eV) Obtained with PBE + U + D2 for $MnPX_{3-n}$ (X = S and Se)

defect type	X = S	X = Se
V_X@1L	1.407	1.177
V_{X2}@1L	1.651	1.493
V_{X2a}@2L	1.551	1.309
V_{X2b}@2L	1.466	1.264

the Se vacancy is more likely to occur compared to the S vacancy, which correlates with the respective electronegativity values. For the same X, the feasibility of defect formation is V_X@1L < V_{X2b}@2L < V_{X2a}@2L < V_{X2}@1L.

A chalcogen vacancy formation leads to a strong modification of the local atomic and electronic structures. Compared to the pristine $MnPX_3$ monolayer, the P−P dimers in all defective structures tend to move toward vacancies and being pulled out from the monolayers, leading to an angle change between the P−P dimer and vertical direction. Among all, the angle of V_{X2b}@2L changed the most (10.56° for V_{S2b}@2L and 13.88° for V_{Se2b}@2L), and the dimer in V_{X2b}@2L remains in its original horizontal position due to the absence of two X on the opposite corner of $[P_2X_6]^{4-}$. The P−X bond length is enlarged, while the P−P bond length is shortened. V_{X2}@1L undergoes the most significant change in P−X bond length (by 0.112 Å for V_{X2}@1L and 0.106 Å for V_{X2}@1L) and P−P bond length (by 0.109 Å for V_{X2}@1L and 0.094 Å for V_{X2}@1L) due to the absence of the two neighboring X atoms of the same chalcogen sublayer.

Upon removal of a chalcogen atom(s), an occupied defect state appears in the density of states (DOS) of the defective monolayer. As follows from the electronic structure of pristine $MnPX_3$, for the electrons left behind upon removal of chalcogen atom(s), the electronic states of a $[P_2X_{6-n}]$-entity and Mn 3d-states are equally accessible. Consequently, the defect states have contributions from P-, X p-, and Mn d-states. At that, for V_X@1L and V_{X2b}@2L, these defect states are not effectively energetically split from the valence band states. Therefore, the energy gap of the defective monolayers in each of these cases is only slightly reduced compared to the pristine $MnPX_3$ (Figure 2c,d,i,j). In contrast, the state formed after the creation of vacancy V_{X2}@1L is well separated from the valence bands (Figure 2e,f), and we can expect the increased reactivity toward water in this case.[37] Formation of this state yields reduction of the band gap with respect to the pristine monolayer for the both X. To shed more light on the nature of this state, we investigated the partial electron distribution for this vacancy type (Figure 3). While the electron density is mostly delocalized between the P and S atoms of the defective sublayer, the d states of the neighboring Mn ions are also affected. It is interesting to note that all defective structures retain the AFM configuration in their ground states except V_{X2a}@2L, which demonstrates the FM behavior (Figure 2g,h).

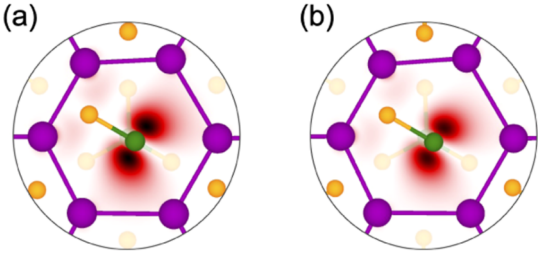

Figure 3. (a,b) Top view of the relaxed structure of defective $MnPX_3$ (X: S and Se) superimposed with the electron densities calculated for the localized defect state in (a) V_{S2}@1L and (b) V_{Se2}@1L.

In the next step, we investigate the adsorption of a single H_2O molecule on pristine $MnPX_3$ (X: S and Se) monolayers. Various high-symmetry adsorption sites and adsorption orientations are considered (see Figures S2 and S3 of the Supporting Information). All adsorption configurations have adsorption energies which range from −90 to −139 meV (Table 2) and from −56 to −168 meV (Table 2) for $MnPS_3$ and $MnPSe_3$, respectively. For $MnPS_3$, the water molecule tends to adsorb directly above an P atom [d(P−O) = 3.37 Å], and H atoms are directed toward the neighboring X atoms [d(H−S) = 2.91/2.86 Å] as it is shown in Figure 4a. Meanwhile, H_2O prefers to adsorb on the hollow site of $MnPSe_3$ with two H atoms interact with two Se atoms [d(H−Se) = 2.838 Å, see Figure S3e of the Supporting Information]. In accordance with the weak interaction, the structural parameters of H_2O as well as of the studied monolayer undergo insignificant changes.

Table 2. Adsorption Energies (E_{ads}, in meV) Obtained with PBE + U + D2 for the Energetically Most Favorable Configurations for Interaction of H_2O on the Pristine and Defective $MnPX_3$ (X = S and Se) Monolayers[a]

	X = S		X = Se	
System	E_{ads}^{mol}	E_{ads}^{dis}	E_{ads}^{mol}	E_{ads}^{diss}
$MnPX_3$	−139	1048	−168	1232
V_X@1L	−645	−539	−745	−574
V_{X2}@1L	−1201	−1279	−1220	−1315
V_{X2a}@2L	−770	−845	−830	−754
V_{X2b}@2L	−735	−662	−835	−819

[a]The molecular and dissociative adsorption modes are considered separately.

To shed more light on the adsorbate mode, we have investigated the electron density redistribution ($\Delta\rho$) upon adsorption (Figure 4a). (The respective data for $MnPSe_3$ are presented in Figure S4a of the Supporting Information.) When molecular water adsorbs on the pristine $MnPX_3$ monolayer, the main charge rearrangement takes place between O and P atoms. Charge accumulation in the p-orbital of P on the side of the adsorbate indicates that it is the main orbital participating in the bonding. The electron density accumulation between H_2O and $MnPX_3$ is accompanied with a depletion at the hydrogen positions. Furthermore, there is a clear signature for the interaction between water hydrogens and the neighboring chalcogen atoms.

The main effects in DOS expected due to the interaction between H_2O and $MnPX_3$ are a shift of position and change in the width of the molecular levels of the adsorbate. Analysis of the partial DOS (Figures 4a and S4a) shows that the bonding to the monolayer is mainly due to the $1b_1$ molecular orbital (MO) of H_2O (the oxygen lone pair). This orbital undergoes some broadening due to hybridization with the p states of P. In addition, a slight upward shift with respect to the MO of the gas phase water molecule is observed for this MO.

Considering the defective monolayers, the situation is more interesting. First, the adsorption structure similar to the one presented in Figure 4a exists. It is presented in Figure 4b (for the $MnPSe_3$ data, see Figure S4b of the Supporting

https://doi.org/10.1021/acsomega.3c04677
ACS Omega 2023, 8, 33920−33927

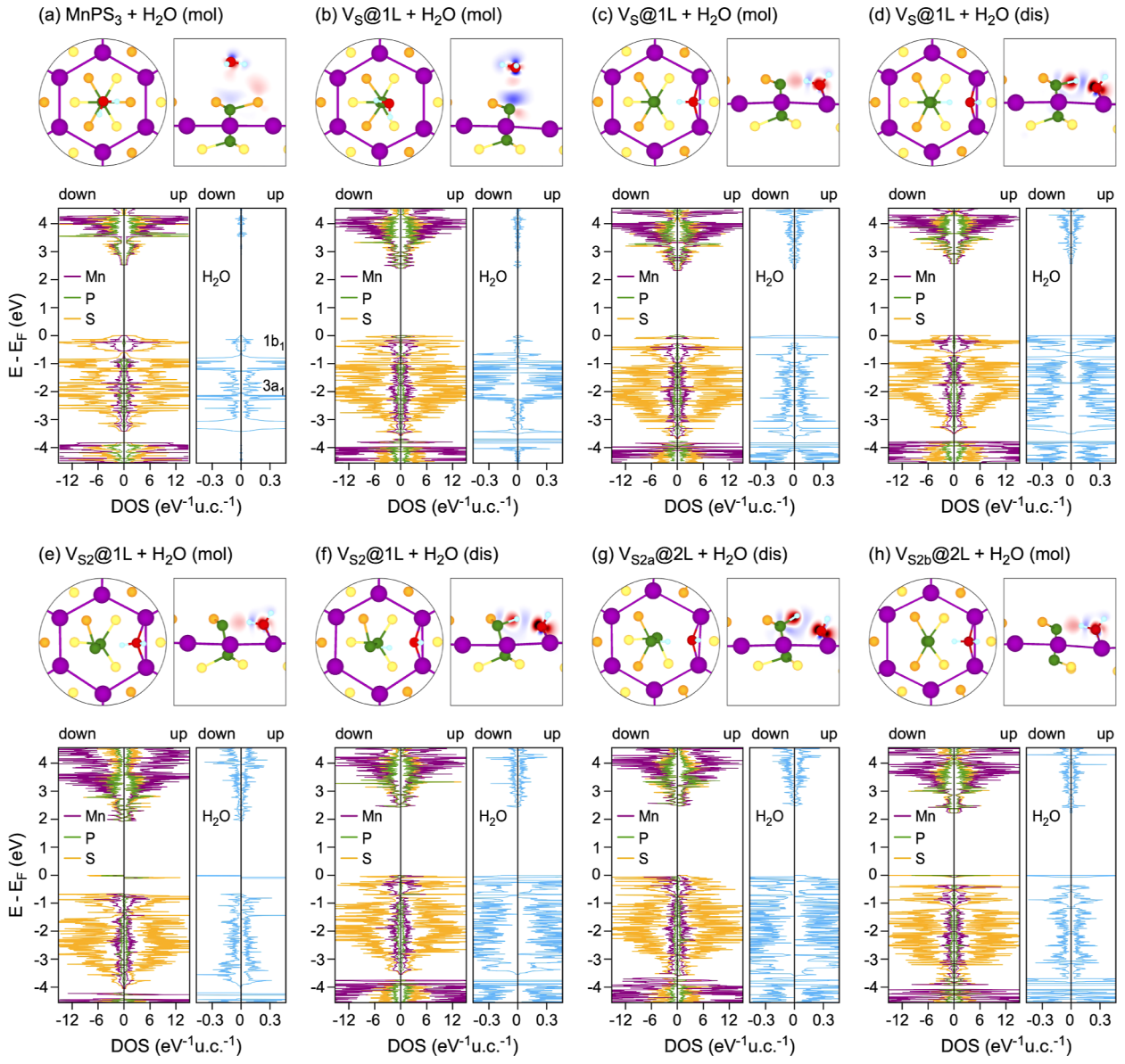

Figure 4. Top and side views of the relaxed structures obtained after water adsorption on pristine and defective $MnPS_3$ (see text for details). Spheres of different size/color represent ions of different types. Side views are superimposed with electron density redistribution maps: $\Delta\rho(r) = \rho_{A/B}(r) - [\rho_A(r) + \rho_B(r)]$ (A: adsorbate; B: substrate). Here, $\Delta\rho(r)$ is color-coded as blue (−0.01 eÅ^{-3})—white (0)—red (+0.01 eÅ^{-3}) in (a,b) and as blue (−0.1 eÅ^{-3})—white (0)—red (+0.1 eÅ^{-3}) in (c−h). Atom-projected DOS obtained with PBE + U + D2 for the above structures.

Information). In this case, the interaction between H_2O and the substrate is stronger (E_{ads} = −180 meV and E_{ads} = −208 meV for $MnPS_3$ and $MnPSe_3$, respectively), which is reflected by the reduced distance of d(P−O) = 2.98 and 3.02 Å for $MnPS_3$ and $MnPSe_3$, respectively. Furthermore, the electronic structures of the molecule and substrate undergo qualitatively similar changes as in the case of the pristine monolayer.

In addition, a structure where the water molecule is coordinated between two Mn ions as it is shown in Figure 4c was investigated. Charge accumulation is observed between O and two Mn atoms as well as between H and P atoms, which lost the chalcogen neighbor (Figures 4c and S4c). A significant contribution of the $1b_1$ and $3a_1$ MOs to the bonding with the monolayer is expressed in their substantial broadening due to hybridization with the P p sates. The healing of vacancy is accompanied by the shift of the defect-derived state from its original position where it is mixed with the valence band states to lower binding energies.

The interaction between H and P atoms in this case has one important effect on the geometric structure: a significant elongation of the H−O bond from 0.97 Å for the gas-phase molecule to 0.98/1.05 and 0.98/1.04 Å for the adsorbed molecule on $MnPS_{3-x}$ and $MnPSe_{3-x}$, respectively. Meanwhile, the interaction between H_2O and the substrate is stronger than the phosphorus site (E_{ads} = −645 and E_{ads} = −745 meV for $MnPS_3$ and $MnPSe_3$, respectively). A further H−O bond elongation up to d(O−H) = 1.54 Å leads to the structure presented in Figure 4d (for the $MnPSe_3$ data, see Figure S4d of the Supporting Information), which is slightly higher in energy as compared to the structure presented in Figure 4) (Table 2). Here, the P−H bond is formed (d(P−H) = 1.47 Å). The weaker adsorbate−substrate interaction in the case of V_S@1L + H_2O (dis) is reflected by less pronounced changes in the

https://doi.org/10.1021/acsomega.3c04677
ACS Omega 2023, 8, 33920−33927

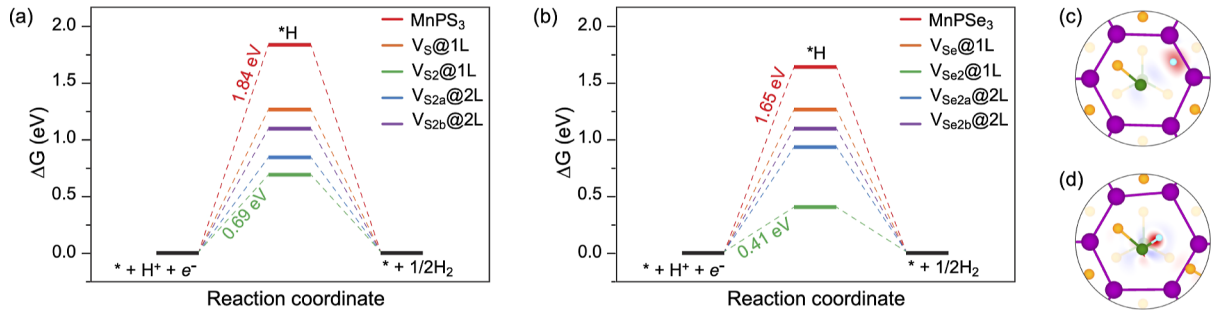

Figure 5. (a,b) Gibbs free energy diagram for HER as obtained for the pristine and defective $MnPX_3$ monolayers as obtained with PBE + U + D2. (c,d) Top views of the relaxed structures obtained after hydrogen atom adsorption on the defective $MnPS_3$ (see the text for details) superimposed with electron density redistribution maps: $\Delta\rho(r) = \rho_{A/B}(r) - [\rho_A(r) + \rho_B(r)]$ (A: adsorbate; B: substrate). Here, $\Delta\rho(r)$ is color-coded as blue (-0.1 eÅ^{-3})—white (0)—red ($+0.1$ eÅ^{-3}).

DOS of the interacting species as compared to V_S@1L + H_2O (mol). By that, the qualitative tendency of the induced modifications in these two cases is similar to each other.

The V_{X2}@1L defect binds the H_2O molecule more strongly (Table 2), which results in broadening of DOS when comparing the results obtained for V_{X2}@1L + H_2O (Figure 4e,f) and V_X@1L + H_2O (Figure 4c,d) for both molecular and dissociative adsorption. It is noteworthy that in the case of V_{S2}@1L, the dissociative adsorption mode is energetically more favorable than the molecular one (Table 2).

It is not surprising that the defects V_{X2a}@2L and V_{X2b}@2L demonstrate the behavior very similar to that of V_X@1L as in all these structures, one chalcogen is missing in the upper layer. By that, the charge density redistribution due to the absence of S or Se in the bottom layer makes the adsorption somewhat stronger for V_{X2a}@2L and V_{X2b}@2L as compared to V_X@1L (Table 2). It is worth to mention that in the case of V_{S2a}@2L, the dissociative adsorption mode is energetically more favorable than the molecular one, although the difference in energy between them is not that pronounced as in the case of V_{S2}@1L. The reason for that is better separation of the defect states from the valence band states for V_{S2}@1L (Figure 2e) compared to V_{S2a}@2L (Figure 2g) and V_{S2b}@2L (Figure 2i).

In the next step, we investigate the catalytic activity of the system for the HER. The overall HER pathway can be described by a three-state diagram comprising an initial state $H^+ + e^-$, an intermediate-adsorbed H*, and a final product $\frac{1}{2}$ H_2. The Gibbs free energy of the intermediate state, $|\Delta G_{H^*}|$, is usually considered as a major descriptor of the HER activity.[44] The optimum value of $|\Delta G_{H^*}|$ should be zero; for instance, this value for the well-known highly efficient Pt catalyst is near-zero as $|\Delta G_{H^*}| \approx 0.09$ eV.[45] In the present work, we probed different adsorption configurations (for details, see the Supporting Information, Figure S5) and choose the one with the lowest energy for each of the structure, and the obtained data are presented in Figure 5. Almost all adsorption configurations show largely positive $|\Delta G_{H^*}|$, indicating very weak H* adsorption and easy product desorption, both of which are unfavorable for electrocatalytic HER. However, V_{X2}@2L with the well-localized defect states show improved efficiency. It is noteworthy that while in the case of V_{S2}@1L the adsorbed H is coordinated between two Mn ions (Figure 5c), a P−H bond is created due to the adsorption of H on the defective $MnPSe_3$ (Figure 5d). The latter modification results in significant lowering of $|\Delta G_{H^*}|$. The obtained results ($|\Delta G_{H^*}| = 0.69$ eV and $|\Delta G_{H^*}| = 0.41$ eV for V_{S2}@2L and V_{Se2}@2L, respectively (Figure 5a,b)), correlate with the experimental data obtained for the $MnPX_3$ flakes, which are in the range between 0.525 and 0.835 V, depending on X.[38,39] Thus, according to the results of our calculations, pristine $MnPX_3$ exhibits significant positive values of $|\Delta G_{H^*}|$, which can be reduced by introducing a defect. To further lower the $|\Delta G_{H^*}|$ value, doping with heteroatoms − metallic and non-metallic − can be used. Consequently, the combination of defects and doping can allow to rationally design $MnPX_3$ with high-throughput HER, which will be subjects of our future studies.

An important property of a catalyst is the maintenance of its activity for a long time. In the studied case, the greatest problem can be caused by poisoning of active sites of the catalyst with the OH groups. Obviously, this threat can only arise in an alkaline media. Therefore, the straightforward solution would be the acidity control. Furthermore, it has been shown previously that rapid desorption of OH groups can be achieved by applying an electrical potential,[46] and, for example, $MnPSe_3$ yields very good stability after 100 cycles for HER in a wide pH range.[41]

CONCLUSIONS

We performed systematic DFT studies of the initial steps of water adsorption on pristine and chalcogen-defective 2D $MnPX_3$ (X: S and Se), which are shown to be narrow gap semiconductors with a Mott−Hubbard-type insulating state. On pristine monolayers, a molecular adsorption is detected unless the chalcogen vacancy is created, and the results obtained for S and Se are almost identical. In the presence of chalcogen vacancies, the water splitting is possible, and the dissociation pathway is strongly promoted upon removal of two X atoms from the same chalcogen layer. This can be explained by the formation of the strongly localized (in space and in energy) defect states in the DOS of the defective monolayers under study. Furthermore, the MPX_3 monolayers with the vacancy of this type (*i.e.*, V_{X2}@1L) show the improved catalytic activity for the HER. Such an elucidation of the structure−activity relationship can provide a deeper understanding of the nature of interaction between 2D materials and water and help in strategy development and synthesis of new HER electrocatalysts.

COMPUTATIONAL DETAILS

The spin-polarized DFT calculations based on plane-wave basis sets were performed with the Vienna Ab Initio Simulation

https://doi.org/10.1021/acsomega.3c04677
ACS Omega 2023, 8, 33920−33927

Package (VASP).[47,48] The Perdew−Burke−Ernzerhof (PBE) exchange−correlation functional[49] was employed. The ion cores were described by projector-augmented wave (PAW) potentials,[50] and the valence electrons [Mn (3p, 3d, 4s), P (3s, 3p), S (3s, 3p), and Se (4s, 4p)] were described by plane waves associated with kinetic energies of up to 500 eV. Brillouin zone integration was performed on Γ-centered symmetry with Monkhorst−Pack meshes by the tetrahedron method with Blöchl corrections.[51] The 12 × 12 × 1 *k*-mesh was used for the (2 × 2) supercells. The DFT + *U* scheme[52,53] was adopted for the treatment of Mn 3d orbitals, with the parameter $U_{eff} = U - J$ equal to 5 eV.[33,43] Dispersion interactions were considered adding a $1/r^6$ atom−atom term as parameterized by Grimme ("D2" parameterization).[54] This approach yields structural parameters, which are in good agreement with available experimental data.[33,43]

When modeling $MnPX_3$ monolayers, the lattice constant in the lateral plane was set according to the optimized lattice constant of bulk $MnPX_3$ (a = 12.142 Å and a = 12.768 Å, for X = S and Se, respectively). A vacuum gap was set to approximately 20 Å. During structure optimization, the convergence criteria for energy and force were set equal to 10^{-5} eV and 10^{-2} eV/Å, respectively.

The electrically neutral vacancies were created by removing one or two X atoms from the (2 × 2) supercells. Thereby, the distance between repeated vacancies in the nearest-neighbor cells is larger than 10 Å. The defect formation energy is defined as follows

$$\Delta E_{def} = \frac{1}{n}[E(MnPX_{3-n}) + n\,\mu_X - E(MnPX_3)]$$

where n is a number of defects atoms, $E(MnPX_{3-n})$ and $E(MnPX_3)$ are the energies of the 2D $MnPX_3$ with and without vacancy, respectively, and μ_X is the chemical potential of X atom (μ_S = −4.1279 eV and μ_{Se} = −3.4895 eV).[43]

To study the adsorption of a single atom or a molecule, a (2 × 2) supercell was used with one hydrogen atom or water molecule added. Adsorption energies were calculated as

$$\Delta E_{ads} = E(A/MnPX_3) - [E(A) + E(MnPX_3)]$$

where $E(MnPX_3)$ and $E(A)$ are the energies of the isolated 2D $MnPX_3$ and an adsorbate and $E(A/MnPX_3)$ is the energy of their interacting assembly.

The catalytic activity in the HER of the system was investigated based on the computational hydrogen electrode (CHE) model proposed by Nørskov *et al.*[44] The free energies have been calculated as

$$\Delta G_H = E_{ads} + \Delta ZPE - T\Delta S_H$$

where ΔZPE is the difference in zero point energy of H between the gaseous and adsorbed states and $T\Delta S_H$ denotes the entropy change of H due to adsorption. Entropy is due to vibration only in the adsorbed state and is much smaller compared to that in the gas phase, where the translational contribution dominates. Therefore, neglecting the vibrational entropy, the changes in the entropy of H ($=\frac{1}{2}$ H_2) under adsorption are determined as $\Delta S_H = \frac{1}{2}S^0(H_2)$ with $S^0(H_2)$ being the entropy of H_2 in the gas phase and tabulated. Previous studies have showed that the value of $\Delta ZPE - T\Delta S \approx 0.24$ eV. Therefore, for the evaluation of the catalytic activity in HER of the system, we used $\Delta G_{H^*} = E_{ads} + 0.24$ eV.[27]

■ ASSOCIATED CONTENT

Supporting Information

The Supporting Information is available free of charge at https://pubs.acs.org/doi/10.1021/acsomega.3c04677.

$MnPX_3$ (X: S and Se) band structures; $H/MnPX_3$ and $H_2O/MnPX_3$ (X: S and Se) adsorption structures; and electron density redistribution maps and site-projected DOS obtained for $H_2O/MnPSe_3$ (PDF)

■ AUTHOR INFORMATION

Corresponding Authors

Jiajun Dai − *Institut für Chemie und Biochemie, Freie Universität Berlin, Berlin 14195, Germany*; Email: daij96@zedat.fu-berlin.de

Elena Voloshina − *Department of Physics, Shanghai University, 200444 Shanghai, P. R. China; Institut für Chemie und Biochemie, Freie Universität Berlin, Berlin 14195, Germany*; orcid.org/0000-0002-1799-1125; Email: elena.voloshina@icloud.com

Yuriy Dedkov − *Department of Physics, Shanghai University, 200444 Shanghai, P. R. China*; orcid.org/0000-0001-7904-2892; Email: yuriy.dedkov@icloud.com

Authors

Kangli Wang − *Physikalisch-Chemisches Institut, Justus-Liebig-Universität Gießen, Gießen 35392, Germany*; orcid.org/0000-0003-2593-1576

Beate Paulus − *Institut für Chemie und Biochemie, Freie Universität Berlin, Berlin 14195, Germany*

Complete contact information is available at: https://pubs.acs.org/10.1021/acsomega.3c04677

Notes

The authors declare no competing financial interest.

■ ACKNOWLEDGMENTS

J.D. acknowledges the China Scholarship Council for the financial support. The computing time granted by the Resource Allocation Board and provided on the supercomputer Lise and Emmy at NHR@ZIB and NHR@Göttingen as part of the NHR infrastructure is gratefully acknowledged. E.V. and Y.D. thank the National Natural Science Foundation of China (grant no. 22272104) for the financial support.

■ REFERENCES

(1) Sun, H.; Edziah, B. K.; Sun, C.; Kporsu, A. K. Institutional Quality, Green Innovation and Energy Efficiency. *Energy Pol.* **2019**, *135*, 111002.

(2) Li, J.; Lai, S.; Chen, D.; Wu, R.; Kobayashi, N.; Deng, L.; Huang, H. A Review on Combustion Characteristics of Ammonia as a Carbon-Free Fuel. *Front. Energy Res.* **2021**, *9*, 760356.

(3) Masao, A.; Noda, S.; Takasaki, F.; Ito, K.; Sasaki, K. Carbon-Free Pt Electrocatalysts Supported on SnO[sub 2] for Polymer Electrolyte Fuel Cells. *Electrochem. Solid-State Lett.* **2009**, *12*, B119.

(4) Abbas, M. A.; Bang, J. H. Rising Again: Opportunities and Challenges for Platinum-Free Electrocatalysts. *Chem. Mater.* **2015**, *27*, 7218−7235.

(5) Anantharaj, S.; Ede, S. R.; Sakthikumar, K.; Karthick, K.; Mishra, S.; Kundu, S. Recent Trends and Perspectives in Electrochemical Water Splitting with an Emphasis on Sulfide, Selenide, and Phosphide Catalysts of Fe, Co, and Ni: A Review. *ACS Catal.* **2016**, *6*, 8069−8097.

(6) Chen, Z.; Wei, W.; Ni, B.-J. Cost-effective Catalysts for Renewable Hydrogen Production via Electrochemical Water Splitting: Recent advances. *Curr. Opin. Green Sustainable Chem* **2021**, *27*, 100398.
(7) Novoselov, K. S.; Geim, A. K.; Morozov, S. V.; Jiang, D.; Zhang, Y.; Dubonos, S. V.; Grigorieva, I. V.; Firsov, A. A. Electric field effect in atomically thin carbon films. *Science* **2004**, *306*, 666−669.
(8) Das, S.; Robinson, J. A.; Dubey, M.; Terrones, H.; Terrones, M. Beyond Graphene: Progress in Novel Two-dimensional Materials and van der Waals Solids. *Annu. Rev. Mater. Res.* **2015**, *45*, 1−27.
(9) Akhtar, M.; Anderson, G.; Zhao, R.; Alruqi, A.; Mroczkowska, J. E.; Sumanasekera, G.; Jasinski, J. B. Recent Advances in Synthesis, Properties, and Applications of Phosphorene. *npj 2D Mater. Appl.* **2017**, *1*, 5.
(10) Khan, K.; Tareen, A. K.; Aslam, M.; Wang, R.; Zhang, Y.; Mahmood, A.; Ouyang, Z.; Zhang, H.; Guo, Z. Recent Developments in Emerging Two-dimensional Materials and Their Applications. *J. Mater. Chem. C* **2020**, *8*, 387−440.
(11) Choudhuri, I.; Bhauriyal, P.; Pathak, B. Recent Advances in Graphene-like 2D Materials for Spintronics Applications. *Chem. Mater.* **2019**, *31*, 8260−8285.
(12) Roy, S.; Zhang, X.; Puthirath, A. B.; Meiyazhagan, A.; Bhattacharyya, S.; Rahman, M. M.; Babu, G.; Susarla, S.; Saju, S. K.; Tran, M. K.; et al. Structure, Properties and Applications of Two-Dimensional Hexagonal Boron Nitride. *Adv. Mater.* **2021**, *33*, 2101589.
(13) Shanmugam, V.; Mensah, R. A.; Babu, K.; Gawusu, S.; Chanda, A.; Tu, Y.; Neisiany, R. E.; Försth, M.; Sas, G.; Das, O. A Review of the Synthesis, Properties, and Applications of 2D Materials. *Part. Part. Syst. Charact.* **2022**, *39*, 2200031.
(14) Jin, H.; Guo, C.; Liu, X.; Liu, J.; Vasileff, A.; Jiao, Y.; Zheng, Y.; Qiao, S.-Z. Emerging Two-dimensional Nanomaterials for Electrocatalysis. *Chem. Rev.* **2018**, *118*, 6337−6408.
(15) Ye, G.; Gong, Y.; Lin, J.; Li, B.; He, Y.; Pantelides, S. T.; Zhou, W.; Vajtai, R.; Ajayan, P. M. Defects Engineered Monolayer MoS_2 for Improved Hydrogen Evolution Reaction. *Nano Lett.* **2016**, *16*, 1097−1103.
(16) Li, X.; Wu, X.; Yang, J. Half-metallicity in $MnPSe_3$ Exfoliated Nanosheet with Carrier Doping. *J. Am. Chem. Soc.* **2014**, *136*, 11065−11069.
(17) Du, K.-z.; Wang, X.-z.; Liu, Y.; Hu, P.; Utama, M. I. B.; Gan, C. K.; Xiong, Q.; Kloc, C. Weak van der Waals Stacking, Wide-range Band Gap, and Raman Study on Ultrathin Layers of Metal Phosphorus Trichalcogenides. *ACS Nano* **2016**, *10*, 1738−1743.
(18) Mukherjee, D.; Austeria, P. M.; Sampath, S. Two-Dimensional, Few-Layer Phosphochalcogenide, $FePS_3$: A New Catalyst for Electrochemical Hydrogen Evolution over Wide pH Range. *ACS Energy Lett.* **2016**, *1*, 367−372.
(19) Wang, F.; Shifa, T. A.; He, P.; Cheng, Z.; Chu, J.; Liu, Y.; Wang, Z.; Wang, F.; Wen, Y.; Liang, L.; et al. Two-dimensional Metal Phosphorus Trisulfide Nanosheet with Solar Hydrogen-evolving Activity. *Nano Energy* **2017**, *40*, 673−680.
(20) Wang, F.; Shifa, T. A.; Yu, P.; He, P.; Liu, Y.; Wang, F.; Wang, Z.; Zhan, X.; Lou, X.; Xia, F.; et al. New Frontiers on van der Waals Layered Metal Phosphorous Trichalcogenides. *Adv. Funct. Mater.* **2018**, *28*, 1802151.
(21) Du, C.-F.; Liang, Q.; Dangol, R.; Zhao, J.; Ren, H.; Madhavi, S.; Yan, Q. Layered Trichalcogenidophosphate: A New Catalyst Family for Water Splitting. *Nano-Micro Lett.* **2018**, *10*, 67.
(22) Mukherjee, D.; Austeria, P. M.; Sampath, S. Few-Layer Iron Selenophosphate, $FePSe_3$: Efficient Electrocatalyst toward Water Splitting and Oxygen Reduction Reactions. *ACS Appl. Energy Mater.* **2018**, *1*, 220−231.
(23) Liang, Q.; Zhong, L.; Du, C.; Luo, Y.; Zheng, Y.; Li, S.; Yan, Q. Achieving Highly Efficient Electrocatalytic Oxygen Evolution with Ultrathin 2D Fe-doped Nickel Thiophosphate Nanosheets. *Nano Energy* **2018**, *47*, 257−265.
(24) Dedkov, Y.; Yan, M.; Voloshina, E. To the Synthesis and Characterization of Layered Metal Phosphorus Triselenides Proposed for Electrochemical Sensing and energy applications. *Chem. Phys. Lett.* **2020**, *754*, 137627.
(25) Xia, X.; Wang, L.; Sui, N.; Colvin, V. L.; Yu, W. W. Recent Progress in Transition Metal Selenide Electrocatalysts for Water Splitting. *Nanoscale* **2020**, *12*, 12249−12262.
(26) Sen, P.; Alam, K.; Das, T.; Banerjee, R.; Chakraborty, S. Combinatorial Design and Computational Screening of Two-Dimensional Transition Metal Trichalcogenide Monolayers: Toward Efficient Catalysts for Hydrogen Evolution Reaction. *J. Phys. Chem. Lett.* **2020**, *11*, 3192−3197.
(27) Das, T.; Alam, K.; Chakraborty, S.; Sen, P. Probing Active Sites on $MnPSe_3$ and $FePSe_3$ Tri-chalcogenides as a Design Strategy for Better Hydrogen Evolution Reaction Catalysts. *Int. J. Hydrogen Energy* **2021**, *46*, 37928−37938.
(28) Sharma, S.; Zeeshan, H. M.; Panahi, M.; Jin, Y.; Yan, M.; Jin, Y.; Li, K.; Zeller, P.; Efimenko, A.; Makarova, A.; et al. Stability of van der Waals $FePX_3$ Materials (X: S, Se) for Water-splitting Applications. *2D Mater* **2023**, *10*, 014008.
(29) Yan, M.; Jin, Y.; Wu, Z.; Tsaturyan, A.; Makarova, A.; Smirnov, D.; Voloshina, E.; Dedkov, Y. Correlations in the Electronic Structure of van der Waals $NiPS_3$ crystals: An x-ray Absorption and Resonant Photoelectron Spectroscopy study. *J. Phys. Chem. Lett.* **2021**, *12*, 2400−2405.
(30) Jin, Y.; Yan, M.; Kremer, T.; Voloshina, E.; Dedkov, Y. Mott−Hubbard Insulating State for the Layered van der Waals $FePX_3$ (X: S, Se) as Revealed by NEXAFS and Resonant Photoelectron Spectroscopy. *Sci. Rep.* **2022**, *12*, 735.
(31) Jin, Y.; Jin, Y.; Li, K.; Yan, M.; Guo, Y.; Zhou, Y.; Preobrajenski, A.; Dedkov, Y.; Voloshina, E. Mixed Insulating State for van der Waals $CoPS_3$. *J. Phys. Chem. Lett.* **2022**, *13*, 10486−10493.
(32) Chittari, B. L.; Park, Y.; Lee, D.; Han, M.; MacDonald, A. H.; Hwang, E.; Jung, J. Electronic and Magnetic Properties of single-layer MPX_3 metal phosphorous trichalcogenides. *Phys. Rev. B* **2016**, *94*, 184428.
(33) Jin, Y.; Yan, M.; Dedkov, Y.; Voloshina, E. Realization of the Electric-field Driven "one-material"-based Magnetic Tunnel Junction Using van der Waals Antiferromagnetic $MnPX_3$ (X: S, Se). *J. Mater. Chem. C* **2022**, *10*, 3812−3818.
(34) Yang, J.; Zhou, Y.; Dedkov, Y.; Voloshina, E. Dirac Fermions in Half-metallic Ferromagnetic Mixed $Cr_{1-x}M_xPSe_3$ Monolayers. *Adv. Theory Simul.* **2020**, *3*, 2000228.
(35) Li, K.; Yan, M.; Jin, Y.; Jin, Y.; Guo, Y.; Voloshina, E.; Dedkov, Y. Dual Character of the Insulating State in the van der Waals $Fe_{1-x}Ni_xPS_3$ Alloyed Compounds. *J. Phys. Chem. Lett.* **2023**, *14*, 57−65.
(36) Xu, S.; Wu, Z.; Dedkov, Y.; Voloshina, E. Adsorption of Water on the Pristine and Defective Semiconducting 2D $CrPX_3$ Monolayers (X: S, Se). *J. Phys. Condens. Matter* **2021**, *33*, 354001.
(37) Wu, Z.; Xu, S.; Zhou, Y.; Guo, Q.; Dedkov, Y.; Voloshina, E. Adsorption of Water Molecules on Pristine and Defective $NiPX_3$ (X: S, Se) Monolayers. *Adv. Theory Simul.* **2021**, *4*, 2100182.
(38) Brotons-Alcázar, I.; Torres-Cavanillas, R.; Morant-Giner, M.; Cvikl, M.; Mañas-Valero, S.; Forment-Aliaga, A.; Coronado, E. Molecular Stabilization of Chemically Exfoliated Bare $MnPS_3$ Layers. *Dalton Trans.* **2021**, *50*, 16281−16289.
(39) Susner, M. A.; Chyasnavichyus, M.; McGuire, M. A.; Ganesh, P.; Maksymovych, P. Metal Thio- and Selenophosphates as Multifunctional van der Waals Layered Materials. *Adv. Mater.* **2017**, *29*, 1602852.
(40) Alam, K.; Das, T.; Chakraborty, S.; Sen, P. Finding the Catalytically Active sites on the Layered Tri-chalcogenide Compounds $CoPS_3$ and $NiPS_3$ for hydrogen evolution reaction. *Phys. Chem. Chem. Phys.* **2021**, *23*, 23967−23977.
(41) Gusmão, R.; Sofer, Z.; Sedmidubsky, D.; Huber, S.; Pumera, M. The Role of the Metal Element in Layered Metal Phosphorus Triselenides upon Their Electrochemical Sensing and Energy Applications. *ACS Catal.* **2017**, *7*, 8159−8170.
(42) Mayorga-Martinez, C. C.; Sofer, Z.; Sedmidubsky, D.; Huber, S.; Eng, A. Y. S.; Pumera, M. Layered Metal Thiophosphite Materials:

https://doi.org/10.1021/acsomega.3c04677
ACS Omega 2023, 8, 33920−33927

Magnetic, Electrochemical, and Electronic Properties. *ACS Appl. Mater. Interfaces* **2017**, *9*, 12563−12573.
(43) Yang, J.; Zhou, Y.; Guo, Q.; Dedkov, Y.; Voloshina, E. Electronic, Magnetic and Optical Properties of $MnPX_3$ (X = S, Se) Monolayers with and without Chalcogen Defects: a First-principles Study. *RSC Adv.* **2020**, *10*, 851−864.
(44) Nørskov, J. K.; Bligaard, T.; Logadottir, A.; Kitchin, J. R.; Chen, J. G.; Pandelov, S.; Stimming, U. Trends in the Exchange Current for Hydrogen Evolution. *J. Electrochem. Soc.* **2005**, *152*, J23−J26.
(45) Zhao, X.; Yang, X.; Singh, D.; Panda, P. K.; Luo, W.; Li, Y.; Ahuja, R. Strain-Engineered Metal-Free h-B_2O Monolayer as a Mechanocatalyst for Photocatalysis and Improved Hydrogen Evolution Reaction. *J. Phys. Chem. C* **2020**, *124*, 7884−7892.
(46) Qi, Y.; Zhang, L.; Sun, L.; Chen, G.; Luo, Q.; Xin, H.; Peng, J.; Li, Y.; Ma, F. Sulfur Doping Enhanced Desorption of Intermediates on NiCoP For Efficient Alkaline Hydrogen Evolution. *Nanoscale* **2020**, *12*, 1985−1993.
(47) Kresse, G.; Furthmüller, J. Efficient Iterative Schemes for ab initio Total-energy Calculations Using a Plane-wave Basis Set. *Phys. Rev. B* **1996**, *54*, 11169−11186.
(48) Kresse, G.; Joubert, D. From Ultrasoft Pseudopotentials to the Projector Augmented-wave Method. *Phys. Rev. B* **1999**, *59*, 1758−1775.
(49) Perdew, J. P.; Burke, K.; Ernzerhof, M. Generalized Gradient Approximation Made Simple. *Phys. Rev. Lett.* **1996**, *77*, 3865−3868.
(50) Blöchl, P. E. Projector Augmented-wave Method. *Phys. Rev. B* **1994**, *50*, 17953−17979.
(51) Blöchl, P. E.; Jepsen, O.; Andersen, O. K. Improved Tetrahedron Method for Brillouin-zone Integrations. *Phys. Rev. B* **1994**, *49*, 16223−16233.
(52) Anisimov, V. I.; Aryasetiawan, F.; Lichtenstein, A. I. First-principles calculations of the electronic structure and spectra of strongly correlated systems: the**LDA**+*U*method. *J. Phys. Condens. Matter* **1997**, *9*, 767−808.
(53) Dudarev, S. L.; Botton, G. A.; Savrasov, S. Y.; Humphreys, C. J.; Sutton, A. P. Electron-energy-loss Spectra and the Structural Stability of Nickel Oxide: An LSDA+U Study. *Phys. Rev. B* **1998**, *57*, 1505−1509.
(54) Grimme, S. Semiempirical GGA-type Density Functional Constructed with a Long-range Dispersion Correction. *J. Comput. Chem.* **2006**, *27*, 1787−1799.

https://doi.org/10.1021/acsomega.3c04677
ACS Omega 2023, 8, 33920−33927